NANO LETTERS

pubs.acs.org/NanoLett Letter

Virus-like Particles Armored by an Endoskeleton

Zhuohong Wu, Jorge L. Bayón, Tatiana B. Kouznetsova, Tetsu Ouchi, Krister J. Barkovich, Sean K. Hsu, Stephen L. Craig, and Nicole F. Steinmetz*

Cite This: https://doi.org/10.1021/acs.nanolett.3c03806 Read Online

ACCESS | Metrics & More | Article Recommendations | Supporting Information

ABSTRACT: Many virus-like particles (VLPs) have good chemical, thermal, and mechanical stabilities compared to those of other biologics. However, their stability needs to be improved for the commercialization and use in translation of VLP-based materials. We developed an endoskeleton-armored strategy for enhancing VLP stability. Specifically, the VLPs of physalis mottle virus (PhMV) and Qβ were used to demonstrate this concept. We built an internal polymer "backbone" using a maleimide−PEG_{15}−maleimide cross-linker to covalently interlink viral coat proteins inside the capsid cavity, while the native VLPs are held together by only noncovalent bonding between subunits. Endoskeleton-armored VLPs exhibited significantly improved thermal stability (95 °C for 15 min), increased resistance to denaturants (i.e., surfactants, pHs, chemical denaturants, and organic solvents), and enhanced mechanical performance. Single-molecule force spectroscopy demonstrated a 6-fold increase in rupture distance and a 1.9-fold increase in rupture force of endoskeleton-armored PhMV. Overall, this endoskeleton-armored strategy provides more opportunities for the development and applications of materials.

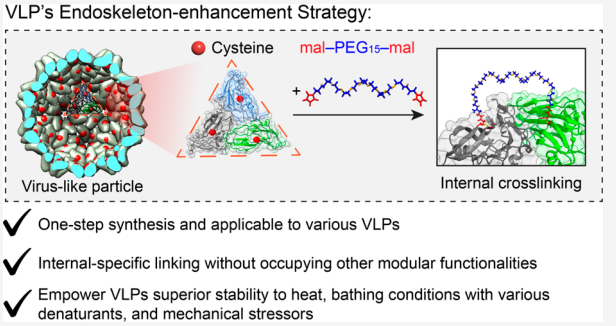

KEYWORDS: *virus-like particles (VLPs), protein cage, stabilization, cross-linking, single-molecule force spectroscopy*

Virus-like nanoparticles (VLPs) are nanomaterials based on the ordered and self-assembled capsids of viruses that lack their infectious genetic material.[2] VLPs are an attractive nanotechnology platform for various discoveries and applications in virology,[3] vaccination,[4,5] bionanotechnology,[6,7] and material science.[8,9] Stabilizing the VLP platform is crucial in ensuring their structural integrity and functionality are maintained during synthesis (e.g., harsh synthesis conditions),[10] storage and shipping,[11,12] and performance (e.g., heat-generating devices).[13,14] Researchers have developed strategies for multiple-point polymer conjugation to the VLP's exterior, but these particles' external chemical functionalities are therefore occupied.[15] Alternatively, the interior of VLPs can be filled with polymers via a stepwise approach or atom-transfer radical polymerization.[16−18] Still, these studies mainly focused on improving the loading capabilities instead of stability (minisurvey in Table S1). As a result, the performance of VLPs stabilized by internal polymeric cross-linkers has yet to be fully understood; the community still lacks a simple yet versatile strategy for stabilizing VLPs.

Multiple VLP platforms have been reviewed elsewhere.[19] Here, we focused on VLPs derived from physalis mottle virus (PhMV) and the bacteriophage Qβ. The PhMV VLP is derived from the +ssRNA virus from the family Tymoviridae, forms an ∼30 nm icosahedral capsid from 180 identical CPs, and can be recombinantly expressed and purified as a homogeneous and stable VLP.[20] The PhMV CP contains one solvent-exposed cysteine residue (C75), internally oriented within the VLP and amenable to alkylation with thiol-reactive small molecules.[21] Qβ VLPs also form T3 icosahedra assembled from 180 identical CPs measuring 28 nm in diameter.[22] The Qβ VLP has two cysteine residues (C74 and C80) per CP that form intersubunit disulfide bonds and link individual CPs into hexameric or pentameric CPs.[23] The disulfide bonds can be reduced and repurposed for chemical conjugation.[24,25] In addition, VLPs feature pores through which cargo can diffuse to access the interior.[26] Although VLPs are not static objects yet dynamic structures, the pore sizes could be estimated. For example, the PhMV VLP possesses pores with diameters of 1.0−1.4 nm[20] and the Qβ VLP possesses large pores of either 1.5 or 3.0 nm.[27]

We set out to develop an endoskeleton-armored strategy for stabilizing VLPs. Specifically, we built an internal VLP "backbone" through covalent inter-CP linking using maleimide−PEG_n−maleimide bivalent cross-linkers, denoted as

Received: October 5, 2023
Revised: January 23, 2024
Accepted: January 24, 2024

https://doi.org/10.1021/acs.nanolett.3c03806
Nano Lett. XXXX, XXX, XXX−XXX

Scheme 1. (a) Chemical Structure and Projected Three-Dimensional Structure of the Maleimide−PEG_{15}−Maleimide Cross-Linker (polymer model created by MolView.org), (b) Side View Showing Its Helical Conformation in Water,[1] (c) Structure of the Physalis Mottle Virus (PhMV) Virus-like Particle (VLP) and Its Coat Protein (CP),[a] (d) Structural Model of PhMV Coat Proteins with a Viral Endoskeleton via Our Endoskeleton-Armored Strategy, Highlighted with Top and Side Views[b]

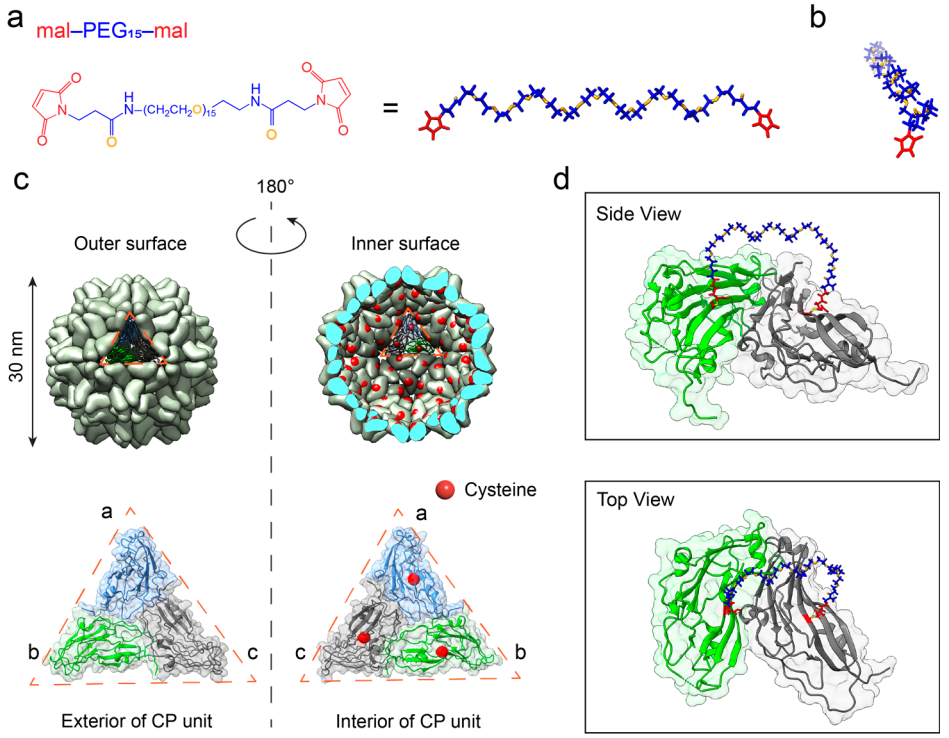

[a]The VLP has an icosahedral $T = 3$ symmetry and is assembled from 180 identical copies of a CP. Three CPs for a triangular unit with a−c (blue, green, and gray, respectively) denoting their position: a in blue clusters at the 5-fold axis with b in green and c in gray at the 2- and 3-fold axes. The internal solvent-exposed cysteine is colored red. The outer size is estimated to be ∼30 nm (PhMV structure created by UCSF Chimera, Protein Data Bank entry 1E57). [b]Notably, the protein−PEG compound in this work is a model to show the idea and does not depict the realistic conformation.

mal−PEG_n−mal (Scheme 1). A combination of gel electrophoresis (native and denaturing), fast protein liquid chromatography (FPLC), dynamic light scattering (DLS), and transmission electron microscopy (TEM) was used to assay and validate the structural properties of the endoskeleton-armored VLPs. Chemical competition assays provided insights into the chemical conjugation efficiency. Endoskeleton-enhanced (EE) VLPs were exposed to various stressors (i.e., surfactants, extreme pHs, chemical denaturants, organic solvents, and mechanical stress) and characterized by a turbidimetric assay, TEM, DLS, and temperature-dependent circular dichroism (CD) spectroscopy. Finally, the mechanical performance was mapped by single-molecule force spectroscopy.

SYNTHESIS AND CHARACTERIZATION OF ENDOSKELETON-ENHANCED (EE) VLPS

We had previously shown that the interior of the PhMV VLP is accessible to small molecules[21,28] and that the internal cysteine residue (C75), even though it is somewhat buried,[29,30] is reactive to maleimide-containing small molecules.[21,31] First, we tested mal−PEG_n−mal cross-linkers of various molecular weights (0.6−5K Da) and numbers of branches (f = 1, 4, and 8). To achieve a high degree of linking, we needed to define a suitable size cutoff (i.e., Flory radius) for the polymer to enter the porous VLP capsid and access the internal cysteine side chains. In addition, it was important to moderate the contour length enabling access to neighboring cysteine residues while avoiding the masking effect; i.e., if the polymer chain is too long, the reactive groups may become buried due to the extra steric hindrance.[32] The end-to-end distance between the sulfur atom of the cysteines on neighboring coat proteins is 27.1−43.9 Å (Figure S1). To determine an optimized synthesis, we first tested mal−PEG_n−mal cross-linkers with different numbers of ethylene glycol repeats (n = 6, 15, 43, and 115, where f is fixed at 1), numbers of branches (f = 1, linear; f = 4 and 8, multiarm), and numbers of equivalents of cross-linker per cysteine (denoted as eq/Cys, i.e., the ratio of the number of mal−PEG_n−mal cross-linkers to the number of cysteines) (Table S2). Upon successful coupling of the mal−PEG_n−mal cross-linker to the VLPs, the succinimide thioether intermediate undergoes ring-opening hydrolysis to add a formal negative charge (Figure 1a).[33,34] The molecular weight of the adduct also increases. Therefore, we used the combination of an electrophoretic mobility shift assay (EMSA) and denaturing sodium dodecyl sulfate−polyacrylamide gel electrophoresis (SDS−PAGE) analysis (Figure 1b,c and Figures S2−S5) to analyze the cross-linked products. The combination of methods has been validated as being reliable for monitoring changes in the molecular weight and charge for modified VLPs.[16,25,35]

The EMSA and SDS−PAGE indicate that the shorter mal−PEG_n−mal cross-linkers (n = 6, 15, and 43; f = 1) resulted in successful linking. When n = 15, the linking is most efficient

https://doi.org/10.1021/acs.nanolett.3c03806
Nano Lett. XXXX, XXX, XXX−XXX

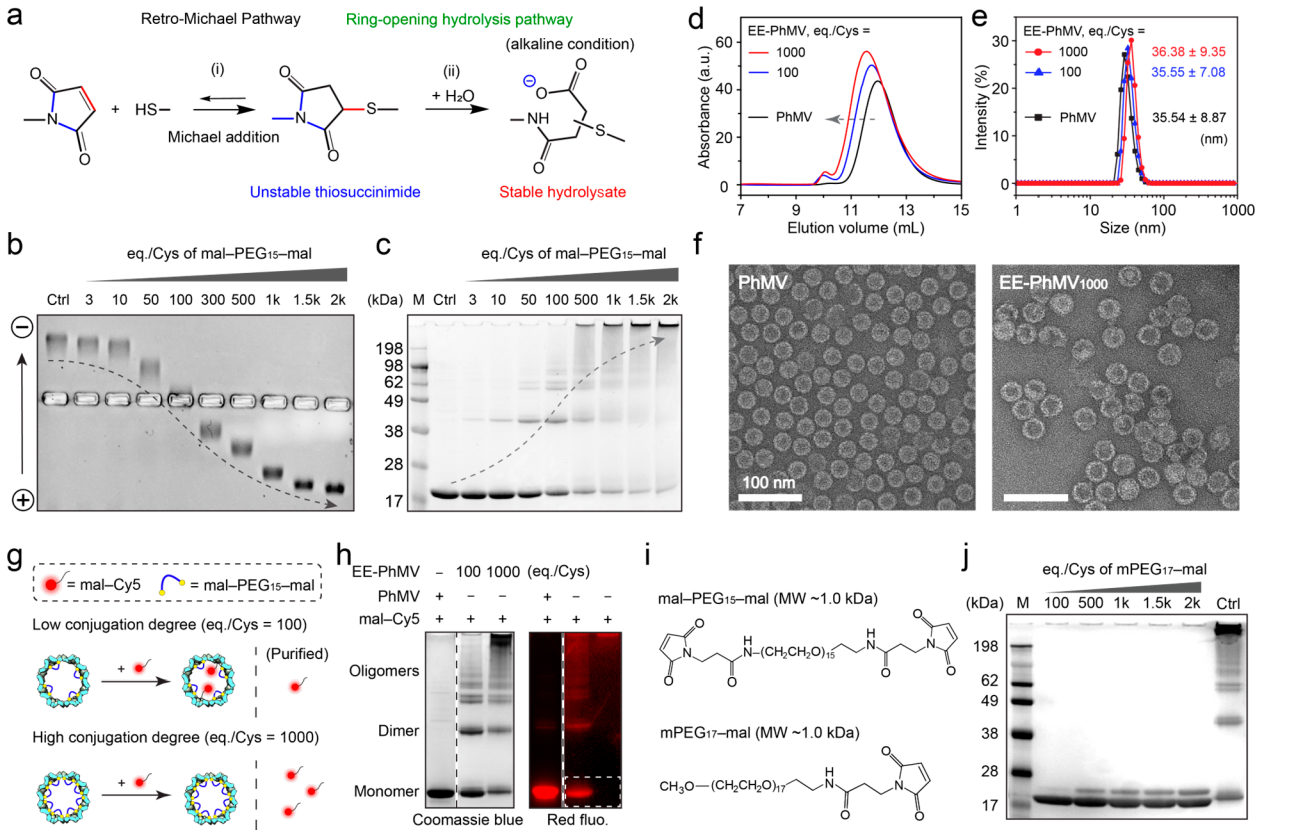

Figure 1. Characterization of endoskeleton-enhanced (EE) PhMV. (a) Michael addition of the thiol to the maleimide results in the maleimide–thiol conjugate, a succinimide thioether. The reaction is fast, but the conjugate is relatively unstable and can undergo further reaction via one of two pathways: (i) a retro-Michael conversion back to the original thiol and maleimide or (ii) an irreversible ring-opening hydrolysis to yield a stable hydrolysate (succinamic acid thioether) under alkaline conditions, which prevents elimination of the maleimide–thiol conjugate and generates a negatively charged and deprotonated carboxylate. This charge change serves as a proxy of the degree of conjugation to the VLPs. (b) Electrophoretic mobility shift assay (EMSA) and (c) denaturing sodium dodecyl sulfate–polyacrylamide gel electrophoresis (SDS–PAGE) image of PhMV and EE-PhMV with various values of eq/Cys. The distance of negative shifting toward the anode positively correlates to the value of eq/Cys. (d) Fast protein liquid chromatography (FPLC) data indicate that the endoskeleton leads to swelling of the VLPs, which agrees with (e) dynamic light scattering (DLS) data. The FPLC detection wavelength is 260 nm. (f) TEM images demonstrate the good dispersity and integrity of native PhMV and EE-PhMV$_{1000}$ (eq/Cys = 1000). (g) Schematic and (h) SDS–PAGE images of the maleimide–Cy5 competition assay. Framed by the white dashed box, the intense fluorescence of EE-PhMV$_{100}$ (eq/Cys = 100) indicates active thiol groups; the absence of fluorescence from the EE-PhMV$_{1000}$ group indicates most reactive thiol groups are occupied by mal–PEG$_{15}$–mal polymers. Complete gels are shown in the Supporting Information. (i) Chemical structures of the mal–PEG$_{15}$–mal and methoxy-PEG$_{17}$–maleimide (mPEG$_{17}$–mal) cross-linkers. (j) SDS–PAGE using the mal–PEG$_{15}$–mal and mPEG$_{17}$–mal cross-linkers. The results indicate that only the mal–PEG$_{15}$–mal cross-linker induces covalent linking within PhMV nanoparticles, thereby ruling out the possibility of physical entanglement. The Ctrl lane represents EE-PhMV$_{1000}$ as a control.

due to the relatively small Flory radius (17.6 Å) and moderate contour length (41.7 Å) (Table S2 and Figure S2). Notably, the longest cross-linker (n = 115; Flory radius = 60.3 Å) is excluded from the VLPs by the gating effect of size-exclusive pores between CPs. The n = 43 cross-linker yielded inefficient labeling, despite being short enough to enter the VLPs (Flory radius = 33.3 Å); its long ethylene glycol chain (contour length = 120 Å) may cause steric hindrance yielding inefficient conjugation. Lastly, when the cross-linker is too short (n = 6; contour length = 16.7 Å) to reach the neighboring cysteine, the linking is proven to be ineffective in the EMSA. Then, we tested multibranch mal–PEG$_n$–mal cross-linkers (f = 4, n = 8; f = 4, n = 25; and f = 8, n = 25) but found that even when the cross-linkers are small enough (Flory radii < 36.6 Å) to enter VLPs, the multibranch mal–PEG$_n$–mal cross-linkers are less reactive than their linear counterparts (Figure S3). The increased rigidity and masking effects can explain this reduced reactivity.

Next, the synthesis is optimized with eq/Cys values ranging from 0 to 2000 by the EMSA and SDS–PAGE analysis. Conjugation is most effective when eq/Cys = 1000. The EMSA shows a characteristic sigmoid curve (Figure 1b) over eq/Cys, plateauing when eq/Cys = 1000. This is consistent with SDS–PAGE analysis showing an increase in the molecular weight of the CP (19.98K Da) to dimers, multimers, and, finally, a higher-molecular weight cross-linked CP assembly that lacks electrophoretic mobility (MW > 198K Da) that plateaued when eq/Cys = 1000 (Figure 1c). The percentage of remaining monomeric bands (i.e., unreacted CP and CP–PEG$_{15}$–mal) at ~20K Da decreases from 100% (eq/Cys = 0) to 14.4% (eq/Cys = 1000), processed by ImageJ (Figure S6).[36] Notably, the band laddering observed via SDS–PAGE cannot be interpreted as the true molecular weight of the CP–polymer conjugates, because the EE-VLPs (especially when eq/Cys > 50) are so stable that the standard denaturation process [1% (w/w) SDS, 95 °C, 5 min] may not be sufficient to denature the VLPs (see Figure 3).

https://doi.org/10.1021/acs.nanolett.3c03806
Nano Lett. XXXX, XXX, XXX–XXX

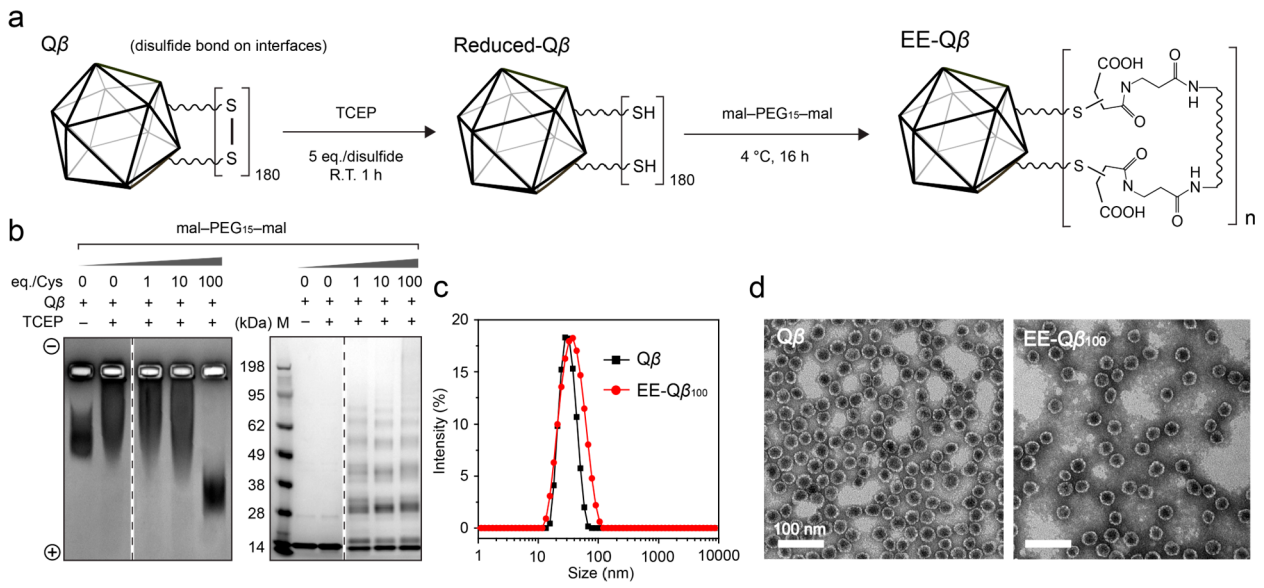

Figure 2. Generalization of the endoskeleton-enhanced strategy tested using Qβ VLPs. (a) Scheme of the reduction of Qβ and rebridging by the mal–PEG_{15}–mal cross-linker with eq/Cys values ranging from 0 to 100 (Protein Data Bank entry 1QBE). Ten equivalents of the reducing agent tris(2-carboxyethyl)phosphine (TCEP) was added to reduce disulfides, followed by rebridging of the mal–PEG_{15}–mal cross-linker at 4 °C for 16 h. (b) EMSA and denaturing SDS–PAGE of native Qβ, reduced Qβ, and reduced Qβ with eq/Cys values of 0–100. (c) DLS and (d) TEM analysis of Qβ and EE-$Q\beta_{100}$ nanohybrids demonstrate the monodispersity and structural integrity of Qβ VLPs and EE-$Q\beta_{100}$.

Nevertheless, the SDS–PAGE analysis agrees with the EMSA and provides insights into the degree of linking of the EE-VLPs. In summary, the linear mal–PEG_{15}–mal telechelic cross-linker (n = 15, f = 1, and eq/Cys = 1000) was adopted for the synthesis of EE-VLPs for further characterization.

After optimizing the synthesis conditions, we analyzed and compared the VLP nanoparticle characteristics of native PhMV, EE-$PhMV_{100}$, and EE-$PhMV_{1000}$. In FPLC, EE-$PhMV_{1000}$, EE-$PhMV_{100}$, and nonmodified PhMV elute at 12.1, 12.4, and 12.9 mL, respectively (Figure 1e). The cross-linkers are contained securely within the VLPs (Figure S7). The shoulder at an elution volume of ~10 mL may represent a small fraction (<5% of the total VLP fraction) of particle doublets or aggregates, possibly due to ultracentrifugation and purification.[17] The DLS results are consistent with FPLC. The hydrodynamic sizes of nonmodified PhMV and EE-$PhMV_{1000}$ are measured by DLS to be 35.54 ± 8.87 and 36.38 ± 9.35 nm in hydrodynamic diameter, respectively, with the reported polydispersity index (PDI) (Figure 1d and Table S5). This ~2.4% size increase may be attributed to PEG cross-linkers protruding through the pores; this has been observed with other VLP–polymer complexes.[18,37] Lastly, TEM images confirmed the good dispersity and morphologic integrity of EE-PhMV VLPs (Figure 1f). Together, the data suggest that mal–PEG_{15}–mal cross-linking of the VLPs does not alter their structural conformation, even at the high degree of internal linking obtained when eq/Cys = 1000.

To determine the degree of conjugation of EE-PhMV, we used a double-conjugation reaction competition assay with the maleimide–cyanine5 cross-linker (mal–Cy5; MW = 605.8 Da). Incomplete cysteine conjugation leaves unoccupied side chains for further reaction with mal–Cy5, resulting in fluorescent CP that can be detected via SDS–PAGE. While there is some fluorescent signal observed for the Cy5-labeled EE-$PhMV_{100}$, no fluorescence was observed with EE-$PhMV_{1000}$, suggesting that a complete reaction with the mal–PEG_{15}–mal linker was indeed achieved (Figure 1g,h, Figure S5, and Table S4). In addition to the fluorescent CP, higher-molecular weight dimers and multimers are apparent. Multimers are often observed when viral CPs are labeled with polymers, because CP–polymer conjugates tend to become physically entangled in SDS–PAGE gels.[38,39] To further ensure that the higher-molecular weight bands are a result of covalent linking and not artifacts from CP–polymer physical entanglement, we reacted VLPs with the monovalent mPEG$_{17}$–mal cross-linker (methoxy-PEG_{17}–maleimide) (Figure 1i,j). The conjugation resulted in an expected size increase with a CP–PEG at ~21 kDa, compared with native CP at ~20 kDa, but higher-order CP adducts are observed. It is interesting to note that the conjugation with the monovalent mPEG$_{17}$–mal cross-linker did not result in complete reaction. This contrasts with the results of the bivalent mal–PEG_{15}–mal cross-linker. We hypothesize that although both linkers undergo steric hindrance within the interior, the improved reactivity of bivalent cross-linkers could be explained by the nanoconfinement effect. That is, once one end is conjugated, the rate of reactivity of the other end increases relatively.[6,40,41]

In addition, to generalize the scope of this EE strategy, we validated this concept in the Qβ VLP targeting cysteines at the interface, namely, C74 and C80. In the native VLP, these residues are covalently linked through disulfide bonds, and we first reduced them to free thiols to render them chemically addressable (Figure 2a). The mal–PEG_{15}–mal cross-linker was then conjugated, following the methods applied to PhMV. The EMSA and SDS–PAGE support chemical linking, which is evident by mobility changes and laddering effects as a function of the reactant ratio (eq/Cys) (Figure 2b and Figure S8). DLS and TEM confirmed that monodisperse and structurally sound EE-$Q\beta_{100}$ was obtained (Figure 2c,d). These data validate that the proposed EE strategy could be applied to various VLPs, even to those with cysteines at their coat protein interfaces.

https://doi.org/10.1021/acs.nanolett.3c03806
Nano Lett. XXXX, XXX, XXX–XXX

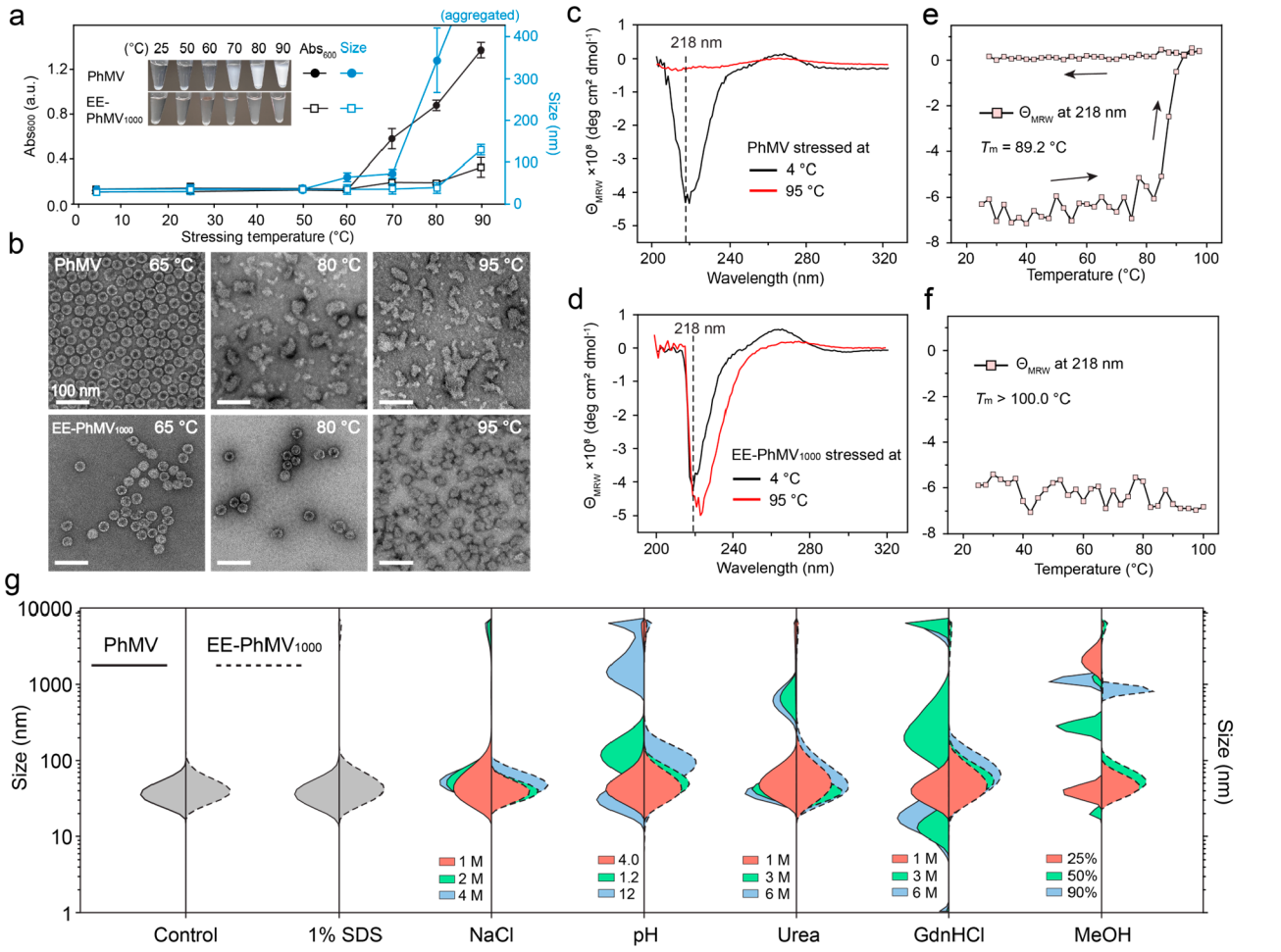

Figure 3. Comprehensive stability assay of PhMV and EE-PhMV. (a) Turbidimetric assay (Abs_{600}, black) and size measurement (blue) for determining the thermally induced aggregation of PhMV (filled circles) and EE-PhMV (empty squares) in the range of 25−90 °C. Both groups appeared as microscale aggregates at 90 °C. Samples at 4 °C are used as a negative control. The inset shows photographs of samples after treatment at different temperatures for 15 min. (b) TEM images show the thermally induced morphological changes of PhMV and EE-PhMV at various temperatures. Circular dichroism (CD) spectra of (c) PhMV and (d) EE-PhMV after thermal stress at 4 °C (negative control) and 95 °C for 15 min. The content of the β-structure is quantified at 218 nm, which is indicated by dashed lines at 218 nm. Θ_{MRW} represents the mean residue weight. Temperature-dependent CD is conducted by monitoring the change in the β-structure of (e) PhMV and (f) EE-PhMV from 25 to 100 °C. (g) Size distribution under miscellaneous stressing conditions, including in the presence of surfactants, salts, pH, chemical denaturants, and organic solvents. DLS samples are triplicate and presented as intensity (percent).

THERMAL STABILITY OF EE-PHMV$_{1000}$

The stability of VLPs, which are macromolecular assemblies of their coat proteins, relies on a delicate balance between short-range, predominantly hydrophobic attraction and long-range electrostatic repulsion,[42,43] which are considered "weak links" due to the nature of noncovalent interactions.[15] Different denaturing conditions, such as extreme temperatures,[15] ionic strengths, acids, bases,[44] surfactants,[45] or chaotropic agents,[14,46] decrease or increase the strength of noncovalent bonds and, therefore, weaken or strengthen, respectively, the coat protein interactions within the VLPs, thus altering stability. The thermal stability of nonmodified PhMV and EE-PhMV was probed in buffered media over a temperature range of 25−90 °C for 15 min. Visual inspection of the test tubes showed clouding of the nonmodified PhMV, and this phenomenon, consistent with protein aggregation and precipitation, was enhanced at higher temperatures (Figure 3a, inset). In stark contrast, the temperature-treated EE-PhMV nanohybrid solutions remained clear. The turbidity was further analyzed by measuring Abs_{600} (Figure 3a);[47,48] the quantitative readout demonstrates that the polymer endoskeleton improves the thermal stability of PhMV VLPs from 50 °C for the nonmodified VLPs to 80 °C for the EE-PhMV. In addition, TEM images show both nanoparticles remain structurally intact at 65 °C. At 80 and 95 °C, the nonmodified PhMV VLPs appear in heterogeneous shapes and irregular sizes due to CP disassembly and reassembly, indicating the loss of structural integrity (Figure 3b). In stark contrast, the EE-PhMV nanohybrids appear to maintain structural integrity; these data indicate that the EE armor increased the thermal stability of the quaternary structure of EE-PhMV relative to that of PhMV VLPs.

Next, to assess the thermal effects on the secondary structure, PhMV and EE-PhMV$_{1000}$ (Figure 3c,d) were analyzed by far-ultraviolet circular dichroism (CD) with thermal stress (95 °C for 15 min) or without (4 °C). The CD spectra of PhMV and EE-PhMV show a maximal ellipticity at 218 nm, characteristic of proteins rich in β-sheet structures,[30,49] which indicates that the introduction of the mal−PEG$_{15}$−mal cross-linker does not affect the β-sheet

https://doi.org/10.1021/acs.nanolett.3c03806
Nano Lett. XXXX, XXX, XXX−XXX

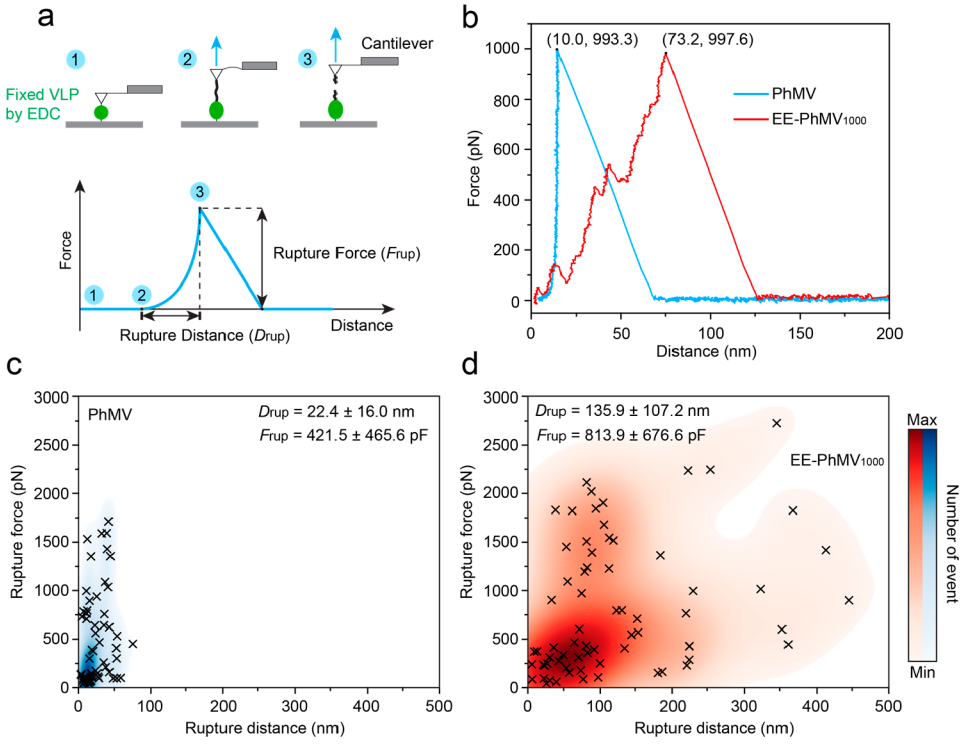

Figure 4. Mechanical performance of PhMV and EE-PhMV. (a) Schematic of the single-molecule force spectroscopy (SMSF) study performed by AFM in the "force−extension" operational mode. The exterior-exposed carboxylates were activated by a 1-ethyl-3-[3-(dimethylamino)propyl]-carbodiimide (EDC) cross-linker, followed by conjugation to an amine-functionalized station and amine-functionalized AFM cantilever. Two critical parameters are schematized: rupture distance (D_{rup}) and rupture force (F_{rup}). (b) Representative force−extension curves of PhMV and EE-PhMV$_{1000}$. (c and d) Statistical mapping shows the two-dimensional distribution of rupture forces and the distances of PhMV and EE-PhMV$_{1000}$. D_{rup} and F_{rup} are increased 6- and 1.9-fold, respectively. The number of events is 71. A p value of <0.05 is statistically significant. Independent sample t test analysis reveals $p < 0.001$ for both rupture force and rupture distance between native PhMV and EE-PhMV$_{1000}$. The statistical data were visualized via Seaborn.[52]

content.[15] After exposure to 95 °C, the nonmodified PhMV loses the signal at 218 nm, while EE-PhMV$_{1000}$ maintains its strong signal. With a fixed-wavelength detection of 218 nm, the β-sheet signals of PhMV and EE-PhMV are monitored within the range of 25−100 °C (Figure 3e,f and Figure S1).[50] The melting temperatures (T_m) of PhMV and EE-PhMV$_{1000}$ are 89.2 and >100 °C, respectively. Denaturation of the intact PhMV is irreversible, as the cooling of denatured PhMV does not result in the recovery of secondary structures. These results support the conclusion that EE-PhMV is highly thermally stable. A potential mechanism is provided (Supplementary Note 1). In summary, this endoskeleton-armored strategy might lead to steric compaction and enhanced attractions between CPs, making EE-VLPs more resistant to the dissociation of both secondary and quaternary structures under various stressors.

COMPREHENSIVE STABILITY OF EE-PHMV$_{1000}$ UNDER VARIOUS DENATURANTS

We tested whether EE-VLP$_{1000}$ would also be more resistant to various chemical denaturants. Nonmodified PhMV and EE-PhMV$_{1000}$ were exposed to SDS [1% (w/v), 24 h, room temperature], NaCl (1−4 M, 6 h), pH (1.2−12, 24 h), urea (1−6 M, 24 h), guanidine hydrochloride (1−6 M, 24 h), and methanol (25−90%, 2 h); pre- and post-treatment samples were analyzed by DLS (Figure 3g and Table S5). Under SDS and NaCl treatment, the size distributions of PhMV and EE-PhMV$_{1000}$ remain roughly unchanged. Stressed by different pHs, urea, and GdnHCl concentrations, the size distributions of PhMV changed dramatically, whereas EE-PhMV remained comparatively stable with minor changes in size. Notably, the size distribution of EE-PhMV$_{1000}$ is only slightly affected at 50% methanol, indicating that stability was enhanced and suggesting that a higher degree of stability may be conferred through a more robust EE strategy for stabilizing the VLPs in organic solvents, which potentially lead to the use of endohedrally catalyst-functionalized cages for catalysis.[51] It is interesting that the stability profile could be enhanced so significantly through a simple bivalent linking strategy; in prior research, the enhanced stability of VLPs was reported through only external multipoint-attachment cross-linkers.[15]

SINGLE-MOLECULE FORCE SPECTROSCOPY OF PHMV AND EE-PHMV$_{1000}$

To assess the mechanical performance of intact PhMV and EE-PhMV$_{1000}$, a single-molecule force spectroscopy (SMFS) study was performed by using AFM at the force−extension operational mode, with a pulling velocity of 1000 nm/s.[53,54] PhMV and EE-PhMV$_{1000}$ each exhibit five exterior-exposed carboxylates (namely, side chains of D58, D83, E39, and E47 and the C-terminus). PhMV or EE-PhMV$_{1000}$ was immobilized on an amine-functional substrate, followed by conjugation to an amine-functionalized AFM cantilever by 1-ethyl-3-[3-(dimethylamino)propyl]carbodiimide (EDC) cross-linker (Figures S10 and S11). The external surface and size of the VLPs determine the coupling of the VLPs to the surface and

https://doi.org/10.1021/acs.nanolett.3c03806
Nano Lett. XXXX, XXX, XXX−XXX

tip and the starting point of force−extension curves, and these characteristics are effectively identical for PhMV and EE-PhMV$_{1000}$. Thus, we attribute any differences in the SMFS force−extension curves to the endoskeleton.

Two key parameters, rupture force (F_{rup}) and rupture distance (D_{rup}), are extracted from the force−extension curves. D_{rup} is the change in tip−substrate separation at which the force returns to zero following either rupture of the particle, detachment of the particle, or another scission event along the analyte.[55,56] It therefore captures any difference in mechanical extension of the VLP that might be facilitated by unfolding of the interconnected CPs (Figure 4a).[57] The key difference is shown in the selected SMFS curves in Figure 4b. The SMFS curve of PhMV reflects a single, smooth extension and rupture event with no evidence of multidomain protein unfolding. The curve is instead consistent with a single distortion/stretching event that culminates in an abrupt dissociation (e.g., that of a tip- or surface-tethered CP from the VLP). In stark contrast, SMFS of EE-PhMV$_{1000}$ shows a sawtooth-like curve that is consistent with a series of multiple mechanical rupture events.[58,59] These characteristics are general for the two analytes; additional examples of pulling events of PhMV and EE-PhMV$_{1000}$ are provided (Figure S12). The data show that the chemical connections between the CPs connect them mechanically, as well, as characterized by the net rupture force and distance that increase due to the sawtooth-like extension caused by mal−PEG$_{15}$−mal linking (Figures S13 and S14).[57] The statistics of F_{rup} and D_{rup} (Figure 4c,d) show increases in both upon endoskeleton formation; D_{rup} increased from 22 ± 16 to 136 ± 107 nm, and F_{rup} increased from 422 ± 466 to 814 ± 677 pN. Notably, the multiple-pulling artifacts from multiple viruses involved in a single pulling event were manually ruled out (Figure S15). Because the total energy absorbed before dissociation is a function of both force and distance achieved by the extended analyte, endoskeleton formation results in a substantial mechanical toughening of the VLPs. The average rupture distance of PhMV (i.e., 24 nm) is considerably shorter than the stored length of one CP [estimated to be ∼73 nm (see eq 1 of the Supporting Information)],[54] which is consistent with an absence of CP unfolding during the dissociation process. A precise physical picture underlying the sawtooth pattern observed in EE-PhMV$_{1000}$ cannot be inferred from the available phenomenological data, but the possible mechanism involves a combination of multiple CP dissociations, where entanglements between the congested and overlapping PEG$_{15}$ linkers prevent simple dissociation of one or two CPs from breaking the mechanical connection between the tip and substrate, which is also observed via SDS−PAGE (Figure 1c). The physical entangling between linked CPs is typically invoked for the aggregation observed in gel electrophoresis, as noted above, so it is reasonable to expect that similar effects are present within the intact, modified VLP. In addition to the extension enabled by multiple CP dissociation events, unfolding of dissociated CPs might allow further extension.

CONCLUSION

To summarize, we have outlined a method for improving the stability and mechanical properties of VLPs; PhMV was used as a test bed, and we also demonstrated the feasibility of the endoskeleton enhancement strategy for Qβ VLPs. The endoskeleton armor is synthesized by covalently linking adjacent CPs using bivalent cross-linkers. Superior stability is conferred through the introduction of covalent bonding of the otherwise noncovalently bonded macromolecular protein assembly. The cross-linkers act as a "backbone" to enhance the overall performance of the VLPs. We highlight several points. (1) The endoskeleton-armored strategy does not occupy the external surface or derivatize motifs, allowing for future modular "add-on" functionalities. (2) The endoskeleton-armored VLPs were significantly more stable to heat, bathing conditions with various denaturants, and mechanical stressors; this provides an opportunity for synthesis and modification under harsh conditions, or integration in devices that may require extreme conditions. (3) The polymer-based endoskeleton allows for the exploration of the quaternary structure's hidden length through single-molecule force spectroscopy. Overall, this endoskeleton strategy provides an armored VLP with an increased stability profile that may find utility in physical virology, biomedicine, or advanced materials.

ASSOCIATED CONTENT

Supporting Information

The Supporting Information is available free of charge at https://pubs.acs.org/doi/10.1021/acs.nanolett.3c03806.

Materials and sample expressions and synthesis, comparison of the EMSA and SDS−PAGE analysis, CD spectral measurements and data from AFM single-molecule force spectroscopy, and analysis of rupture force and rupture distance data (PDF)

AUTHOR INFORMATION

Corresponding Author

Nicole F. Steinmetz − *Department of NanoEngineering, University of California, San Diego, La Jolla, California 92093, United States; Center for Nano-ImmunoEngineering, Moores Cancer Center, Shu and K. C. Chien and Peter Farrell Collaboratory, Department of Radiology, Department of Molecular Biology, Department of Bioengineering, Institute for Materials Discovery and Design, and Center for Engineering in Cancer, Institute for Engineering in Medicine, University of California, San Diego, La Jolla, California 92093, United States;* orcid.org/0000-0002-0130-0481; Email: nsteinmetz@ucsd.edu

Authors

Zhuohong Wu − *Department of NanoEngineering, University of California, San Diego, La Jolla, California 92093, United States; Center for Nano-ImmunoEngineering, Moores Cancer Center, and Shu and K. C. Chien and Peter Farrell Collaboratory, University of California, San Diego, La Jolla, California 92093, United States;* orcid.org/0000-0002-5318-9092

Jorge L. Bayón − *Department of NanoEngineering, University of California, San Diego, La Jolla, California 92093, United States; Center for Nano-ImmunoEngineering, Moores Cancer Center, and Shu and K. C. Chien and Peter Farrell Collaboratory, University of California, San Diego, La Jolla, California 92093, United States;* orcid.org/0000-0001-5456-5179

Tatiana B. Kouznetsova − *Department of Chemistry, Duke University, Durham, North Carolina 27708, United States*

Tetsu Ouchi − *Department of Chemistry, Duke University, Durham, North Carolina 27708, United States;* orcid.org/0000-0002-4054-9028

https://doi.org/10.1021/acs.nanolett.3c03806
Nano Lett. XXXX, XXX, XXX−XXX

Krister J. Barkovich − *Center for Nano-ImmunoEngineering, Moores Cancer Center, Shu and K. C. Chien and Peter Farrell Collaboratory, and Department of Radiology, University of California, San Diego, La Jolla, California 92093, United States*

Sean K. Hsu − *Center for Nano-ImmunoEngineering, Moores Cancer Center, Shu and K. C. Chien and Peter Farrell Collaboratory, and Department of Molecular Biology, University of California, San Diego, La Jolla, California 92093, United States;* orcid.org/0000-0003-4592-703X

Stephen L. Craig − *Department of Chemistry, Duke University, Durham, North Carolina 27708, United States;* orcid.org/0000-0002-8810-0369

Complete contact information is available at: https://pubs.acs.org/10.1021/acs.nanolett.3c03806

Author Contributions

N.F.S. and S.L.C. designed and supervised the research. Z.W. performed the synthesis and main experiments. T.B.K. performed the AFM measurements. Z.W., J.L.B., K.J.B., T.O., and S.K.H. analyzed the data and provided input. Z.W. wrote the first drafts of the manuscript. N.F.S. revised the manuscript, and all of the authors discussed the results and read and edited the manuscript.

Notes

The authors declare the following competing financial interest(s): N.F.S. is a co-founder of, has equity in, and has a financial interest with Mosaic ImmunoEnginering Inc. N.F.S. is a co-founder of and serves as manager of Pokometz Scientific LLC, under which she is a paid consultant to Mosaic ImmunoEngineering Inc., Flagship Labs 95 Inc., and Arana Biosciences Inc. The other authors declare no potential conflict of interest.

■ ACKNOWLEDGMENTS

This work was supported by the National Science Foundation Center for the Chemistry of Molecularly Optimized Networks (MONET) (CHE-2116298). This work was performed in part at the San Diego Nanotechnology Infrastructure (SDNI) of the University of California, San Diego, a member of the National Nanotechnology Coordinated Infrastructure (NNCI), which is supported by the National Science Foundation (Grant ECCS-1542148). The electron microscopic images were taken in the Cellular and Molecular Medicine Electron microscopy core facility, which is supported in part by National Institutes of Health Grant S10OD023527.

■ REFERENCES

(1) Oesterhelt, F.; Rief, M.; Gaub, H. E. Single molecule force spectroscopy by AFM indicates helical structure of poly(ethyleneglycol) in water. *New J. Phys.* **1999**, *1*, 6.

(2) Jeevanandam, J.; Pal, K.; Danquah, M. K. Virus-like nanoparticles as a novel delivery tool in gene therapy. *Biochimie* **2019**, *157*, 38−47.

(3) Bruinsma, R. F.; Wuite, G. J. L.; Roos, W. H. Physics of viral dynamics. *Nat. Rev. Phys.* **2021**, *3*, 76−91.

(4) Chung, Y. H.; Church, D.; Koellhoffer, E. C.; Osota, E.; Shukla, S.; Rybicki, E. P.; Pokorski, J. K.; Steinmetz, N. F. Integrating plant molecular farming and materials research for next-generation vaccines. *Nat. Rev. Mater.* **2022**, *7*, 372−388.

(5) Shin, M. D.; Shukla, S.; Chung, Y. H.; Beiss, V.; Chan, S. K.; Ortega-Rivera, O. A.; Wirth, D. M.; Chen, A.; Sack, M.; Pokorski, J. K.; Steinmetz, N. F. COVID-19 vaccine development and a potential nanomaterial path forward. *Nat. Nanotechnol.* **2020**, *15*, 646−655.

(6) Edwardson, T. G. W.; Levasseur, M. D.; Tetter, S.; Steinauer, A.; Hori, M.; Hilvert, D. Protein Cages: From Fundamentals to Advanced Applications. *Chem. Rev.* **2022**, *122*, 9145−9197.

(7) Rother, M.; Nussbaumer, M. G.; Renggli, K.; Bruns, N. Protein cages and synthetic polymers: a fruitful symbiosis for drug delivery applications, bionanotechnology and materials science. *Chem. Soc. Rev.* **2016**, *45*, 6213−6249.

(8) Li, L.; Chen, G. Precise Assembly of Proteins and Carbohydrates for Next-Generation Biomaterials. *J. Am. Chem. Soc.* **2022**, *144*, 16232−16251.

(9) Douglas, T.; Young, M. Viruses: Making friends with old foes. *Science* **2006**, *312*, 873−875.

(10) Renggli, K.; Nussbaumer, M. G.; Urbani, R.; Pfohl, T.; Bruns, N. A chaperonin as protein nanoreactor for atom-transfer radical polymerization. *Angew. Chem., Int. Ed.* **2014**, *53*, 1443−1447.

(11) Riccò, R.; Liang, W.; Li, S.; Gassensmith, J. J.; Caruso, F.; Doonan, C.; Falcaro, P. Metal-Organic Frameworks for Cell and Virus Biology: A Perspective. *ACS Nano* **2018**, *12*, 13−23.

(12) Shin, M. D.; Jung, E. K. Y.; Moreno-Gonzalez, M. A.; Ortega-Rivera, O. A.; Steinmetz, N. F. Pluronic F127 "nanoarmor" for stabilization of Cowpea mosaic virus immunotherapy. *Bioeng. Transl. Med.* **2024**, *9*, e10574.

(13) Lee, P. W.; Shukla, S.; Wallat, J. D.; Danda, C.; Steinmetz, N. F.; Maia, J.; Pokorski, J. K. Biodegradable Viral Nanoparticle/Polymer Implants Prepared via Melt-Processing. *ACS Nano* **2017**, *11*, 8777−8789.

(14) Luzuriaga, M. A.; Welch, R. P.; Dharmarwardana, M.; Benjamin, C. E.; Li, S.; Shahrivarkevishahi, A.; Popal, S.; Tuong, L. H.; Creswell, C. T.; Gassensmith, J. J. Enhanced Stability and Controlled Delivery of MOF-Encapsulated Vaccines and Their Immunogenic Response In Vivo. *ACS Appl. Mater. Interfaces* **2019**, *11*, 9740−9746.

(15) Manzenrieder, F.; Luxenhofer, R.; Retzlaff, M.; Jordan, R.; Finn, M. G. Stabilization of virus-like particles with poly(2-oxazoline)s. *Angew. Chem., Int. Ed.* **2011**, *50*, 2601−2605.

(16) Lucon, J.; Qazi, S.; Uchida, M.; Bedwell, G. J.; LaFrance, B.; Prevelige, P. E., Jr.; Douglas, T. Use of the interior cavity of the P22 capsid for site-specific initiation of atom-transfer radical polymerization with high-density cargo loading. *Nat. Chem.* **2012**, *4*, 781−788.

(17) Abedin, M. J.; Liepold, L.; Suci, P.; Young, M.; Douglas, T. Synthesis of a Cross-Linked Branched Polymer Network in the Interior of a Protein Cage. *J. Am. Chem. Soc.* **2009**, *131*, 4346−4354.

(18) Hovlid, M. L.; Lau, J. L.; Breitenkamp, K.; Higginson, C. J.; Laufer, B.; Manchester, M.; Finn, M. G. Encapsidated atom-transfer radical polymerization in Qbeta virus-like nanoparticles. *ACS Nano* **2014**, *8*, 8003−8014.

(19) Rohovie, M. J.; Nagasawa, M.; Swartz, J. R. Virus-like particles: Next-generation nanoparticles for targeted therapeutic delivery. *Bioeng. Transl. Med.* **2017**, *2*, 43−57.

(20) Sastri, M.; Kekuda, R.; Gopinath, K.; Kumar, C. T. R.; Jagath, J. R.; Savithri, H. S. Assembly of physalis mottle virus capsid protein in Escherichia coli and the role of amino and carboxy termini in the formation of the icosahedral particles. *J. Mol. Biol.* **1997**, *272*, 541−552.

(21) Masarapu, H.; Patel, B. K.; Chariou, P. L.; Hu, H.; Gulati, N. M.; Carpenter, B. L.; Ghiladi, R. A.; Shukla, S.; Steinmetz, N. F. Physalis Mottle Virus-Like Particles as Nanocarriers for Imaging Reagents and Drugs. *BIOMACROMOLECULES* **2017**, *18*, 4141−4153.

(22) Chung, Y. H.; Cai, H.; Steinmetz, N. F. Viral nanoparticles for drug delivery, imaging, immunotherapy, and theranostic applications. *Adv. Drug Deliver Rev.* **2020**, *156*, 214−235.

(23) Golmohammadi, R.; Fridborg, K.; Bundule, M.; Valegård, K.; Liljas, L. The crystal structure of bacteriophage Q-beta at 3.5 Å resolution. *Structure* **1996**, *4*, 543−554.

(24) Chen, Z.; Detvo, S. T.; Pham, E.; Gassensmith, J. J. Making Conjugation-induced Fluorescent PEGylated Virus-like Particles by

Dibromomaleimide-disulfide Chemistry. *J. Visualized Exp.* **2018**, *135*, e57712.
(25) Chen, Z.; Li, N.; Chen, L.; Lee, J.; Gassensmith, J. J. Dual Functionalized Bacteriophage Qbeta as a Photocaged Drug Carrier. *Small* **2016**, *12*, 4563−4571.
(26) Hooker, J. M.; Kovacs, E. W.; Francis, M. B. Interior surface modification of bacteriophage MS2. *J. Am. Chem. Soc.* **2004**, *126*, 3718−3719.
(27) Benjamin, C. E.; Chen, Z.; Kang, P. Y.; Wilson, B. A.; Li, N.; Nielsen, S. O.; Qin, Z. P.; Gassensmith, J. J. Site-Selective Nucleation and Size Control of Gold Nanoparticle Photothermal Antennae on the Pore Structures of a Virus. *J. Am. Chem. Soc.* **2018**, *140*, 17226−17233.
(28) Hu, H.; Masarapu, H.; Gu, Y. N.; Zhang, Y. F.; Yu, X.; Steinmetz, N. F. Physalis Mottle Virus-like Nanoparticles for Targeted Cancer Imaging. *ACS Appl. Mater. Interfaces* **2019**, *11*, 18213−18223.
(29) Krishna, S. S.; Sastri, M.; Savithri, H. S.; Murthy, M. R. Structural studies on the empty capsids of Physalis mottle virus. *J. Mol. Biol.* **2001**, *307*, 1035−1047.
(30) Krishna, S.S.; Hiremath, C.N.; Munshi, S.K.; Prahadeeswaran, D.; Sastri, M.; Savithri, H.S.; Murthy, M.R.N. Three-dimensional Structure of Physalis Mottle Virus: Implications for the Viral Assembly. *J. Mol. Biol.* **1999**, *289*, 919−934.
(31) Barkovich, K. J.; Wu, Z.; Zhao, Z.; Simms, A.; Chang, E. Y.; Steinmetz, N. F. Physalis Mottle Virus-Like Nanocarriers with Expanded Internal Loading Capacity. *Bioconjugate Chem.* **2023**, *34*, 1585−1595.
(32) Rahme, K.; Chen, L.; Hobbs, R. G.; Morris, M. A.; O'Driscoll, C.; Holmes, J. D. PEGylated gold nanoparticles: polymer quantification as a function of PEG lengths and nanoparticle dimensions. *Rsc Adv.* **2013**, *3*, 6085−6094.
(33) Tumey, L. N.; Charati, M.; He, T.; Sousa, E.; Ma, D.; Han, X.; Clark, T.; Casavant, J.; Loganzo, F.; Barletta, F.; Lucas, J.; Graziani, E. I. Mild method for succinimide hydrolysis on ADCs: impact on ADC potency, stability, exposure, and efficacy. *Bioconjugate Chem.* **2014**, *25*, 1871−1880.
(34) Huang, W.; Wu, X.; Gao, X.; Yu, Y.; Lei, H.; Zhu, Z.; Shi, Y.; Chen, Y.; Qin, M.; Wang, W.; Cao, Y. Maleimide-thiol adducts stabilized through stretching. *Nat. Chem.* **2019**, *11*, 310−319.
(35) Kostiainen, M. A.; Hiekkataipale, P.; de la Torre, J. Á.; Nolte, R. J. M.; Cornelissen, J. J. L. M. Electrostatic self-assembly of virus-polymer complexes. *J. Mater. Chem.* **2011**, *21*, 2112−2117.
(36) Schindelin, J.; Arganda-Carreras, I.; Frise, E.; Kaynig, V.; Longair, M.; Pietzsch, T.; Preibisch, S.; Rueden, C.; Saalfeld, S.; Schmid, B.; Tinevez, J. Y.; White, D. J.; Hartenstein, V.; Eliceiri, K.; Tomancak, P.; Cardona, A. Fiji: an open-source platform for biological-image analysis. *Nat. Methods* **2012**, *9*, 676−682.
(37) Lucon, J.; Edwards, E.; Qazi, S.; Uchida, M.; Douglas, T. Atom transfer radical polymerization on the interior of the P22 capsid and incorporation of photocatalytic monomer crosslinks. *Eur. Polym. J.* **2013**, *49*, 2976−2985.
(38) Wu, Z.; Zhou, J.; Nkanga, C. I.; Jin, Z.; He, T.; Borum, R. M.; Yim, W.; Zhou, J.; Cheng, Y.; Xu, M.; Steinmetz, N. F.; Jokerst, J. V. One-Step Supramolecular Multifunctional Coating on Plant Virus Nanoparticles for Bioimaging and Therapeutic Applications. *ACS Appl. Mater. Interfaces* **2022**, *14*, 13692−13702.
(39) Ma, Y.; Wu, Z.; Steinmetz, N. F. In Vitro and Ex Planta Gold-Bonded and Gold-Mineralized Tobacco Mosaic Virus. *Langmuir* **2023**, *39*, 11238−11244.
(40) Grommet, A. B.; Feller, M.; Klajn, R. Chemical reactivity under nanoconfinement. *Nat. Nanotechnol.* **2020**, *15*, 256−271.
(41) Ravasco, J.; Faustino, H.; Trindade, A.; Gois, P. M. P. Bioconjugation with Maleimides: A Useful Tool for Chemical Biology. *Chem. - Eur. J.* **2019**, *25*, 43−59.
(42) Tresset, G.; Chen, J. Z.; Chevreuil, M.; Nhiri, N.; Jacquet, E.; Lansac, Y. Two-Dimensional Phase Transition of Viral Capsid Gives Insights into Subunit Interactions. *Phys. Rev. Applied* **2017**, *7*, 014005.
(43) Chevreuil, M.; Law-Hine, D.; Chen, J.; Bressanelli, S.; Combet, S.; Constantin, D.; Degrouard, J.; Möller, J.; Zeghal, M.; Tresset, G. Nonequilibrium self-assembly dynamics of icosahedral viral capsids packaging genome or polyelectrolyte. *Nat. Commun.* **2018**, *9*, 3071.
(44) Berardi, A.; Evans, D. J.; Baldelli Bombelli, F.; Lomonossoff, G. P. Stability of plant virus-based nanocarriers in gastrointestinal fluids. *Nanoscale* **2018**, *10*, 1667−1679.
(45) Han, Y.; Lin, Z.; Zhou, J.; Yun, G.; Guo, R.; Richardson, J. J.; Caruso, F. Polyphenol-Mediated Assembly of Proteins for Engineering Functional Materials. *Angew. Chem., Int. Ed.* **2020**, *59*, 15618−15625.
(46) Rashid, F.; Sharma, S.; Bano, B. Comparison of guanidine hydrochloride (GdnHCl) and urea denaturation on inactivation and unfolding of human placental cystatin (HPC). *Protein J.* **2005**, *24*, 283−292.
(47) Lee, P. W.; Isarov, S. A.; Wallat, J. D.; Molugu, S. K.; Shukla, S.; Sun, J. E.; Zhang, J.; Zheng, Y.; Lucius Dougherty, M.; Konkolewicz, D.; Stewart, P. L.; Steinmetz, N. F.; Hore, M. J.; Pokorski, J. K. Polymer Structure and Conformation Alter the Antigenicity of Virus-like Particle-Polymer Conjugates. *J. Am. Chem. Soc.* **2017**, *139*, 3312−3315.
(48) Shin, M.; Lee, H. A.; Lee, M.; Shin, Y.; Song, J. J.; Kang, S. W.; Nam, D. H.; Jeon, E. J.; Cho, M.; Do, M.; Park, S.; Lee, M. S.; Jang, J. H.; Cho, S. W.; Kim, K. S.; Lee, H. Targeting protein and peptide therapeutics to the heart via tannic acid modification. *Nat. Biomed. Eng.* **2018**, *2*, 304−317.
(49) Greenfield, N. J. Using circular dichroism spectra to estimate protein secondary structure. *Nat. Protoc.* **2006**, *1*, 2876−2890.
(50) Greenfield, N. J. Using circular dichroism collected as a function of temperature to determine the thermodynamics of protein unfolding and binding interactions. *Nat. Protoc.* **2006**, *1*, 2527−2535.
(51) Brown, C. M.; Lundberg, D. J.; Lamb, J. R.; Kevlishvili, I.; Kleinschmidt, D.; Alfaraj, Y. S.; Kulik, H. J.; Ottaviani, M. F.; Oldenhuis, N. J.; Johnson, J. A. Endohedrally Functionalized Metal-Organic Cage-Cross-Linked Polymer Gels as Modular Heterogeneous Catalysts. *J. Am. Chem. Soc.* **2022**, *144*, 13276−13284.
(52) Waskom, M. seaborn: statistical data visualization. *J. Open Source Softw.* **2021**, *6*, 3021.
(53) Muller, D. J.; Dumitru, A. C.; Lo Giudice, C.; Gaub, H. E.; Hinterdorfer, P.; Hummer, G.; De Yoreo, J. J.; Dufrene, Y. F.; Alsteens, D. Atomic Force Microscopy-Based Force Spectroscopy and Multiparametric Imaging of Biomolecular and Cellular Systems. *Chem. Rev.* **2021**, *121*, 11701−11725.
(54) Mora, M.; Stannard, A.; Garcia-Manyes, S. The nanomechanics of individual proteins. *Chem. Soc. Rev.* **2020**, *49*, 6816−6832.
(55) Arkhipov, A.; Roos, W. H.; Wuite, G. J.; Schulten, K. Elucidating the mechanism behind irreversible deformation of viral capsids. *Biophys. J.* **2009**, *97*, 2061−2069.
(56) Snijder, J.; Uetrecht, C.; Rose, R. J.; Sanchez-Eugenia, R.; Marti, G. A.; Agirre, J.; Guerin, D. M.; Wuite, G. J.; Heck, A. J.; Roos, W. H. Probing the biophysical interplay between a viral genome and its capsid. *Nat. Chem.* **2013**, *5*, 502−509.
(57) Zuo, J.; Li, H. Two-Molecule Force Spectroscopy on Proteins. *ACS Nano* **2023**, *17*, 7872−7880.
(58) Li, H. B.; Oberhauser, A. F.; Fowler, S. B.; Clarke, J.; Fernandez, J. M. Atomic force microscopy reveals the mechanical design of a modular protein. *Proc. Natl. Acad. Sci. U.S.A.* **2000**, *97*, 6527−6531.
(59) Oberhauser, A. F.; Marszalek, P. E.; Erickson, H. P.; Fernandez, J. M. The molecular elasticity of the extracellular matrix protein tenascin. *Nature* **1998**, *393*, 181−185.

https://doi.org/10.1021/acs.nanolett.3c03806
Nano Lett. XXXX, XXX, XXX−XXX